Journal of Geophysical Research - Planets

Shock Vaporization of Silica and the Thermodynamics of Giant Impact Events

Online Auxiliary Materials

R. G. Kraus[1], S. T. Stewart[1], D. C. Swift[2], C. A. Bolme[3], R. Smith[2], S. Hamel[2], B. D. Hammel[2], D. K. Spaulding[4], D. G. Hicks[2], J. H. Eggert[2], and G. W. Collins[2]

[1]Department of Earth and Planetary Sciences, Harvard University, Cambridge, Massachusetts, USA

[2]Lawrence Livermore National Laboratory, Physics Division, Livermore, California, USA

[3]Los Alamos National Laboratory, Physics Division, Los Alamos, New Mexico, USA

[4]Department of Earth and Planetary Sciences, U.C. Berkeley, Berkeley, California, USA

The auxiliary material for this article contains supplemental text, figures, and tables:

S1. Heat capacity of stishovite.
S2. Revised boiling point for SiO_2.
S3. Streaked optical pyrometer (SOP) calibration.
S4. Absorbance of silica fluid.

Figure S.1 Reference Entropy States.
Figure S.2 Spectral response of the SOP.
Figure S.3 Error estimate in SOP calibration.
Figure S.4 Raw and reduced data used in SOP calibration.
Figure S.5 SOP calibration.
Figure S.6 Semiconductor Drude model fit for absorbance of silica.

Table S.1 Summary of variables and annotations in the Auxiliary Materials.
Table S.2 Transition enthalpies for quartz to fused quartz and stishovite.
Table S.3 Kieffer model parameters for stishovite.
Table S.4 Grüneisen parameter estimates for silica liquid.
Table S.5 Revised liquid–vapor curve for silica.

S1. Heat capacity of stishovite

To treat the anisotropy of crystals and accurately model the dispersion relation near the Brillouin zone boundary, Kieffer [1979] proposed a vibrational density of states for the acoustic modes in a crystal of the form,

$$g(\omega)d\omega = \sum_{t=1}^{3} \frac{3N_{\mathrm{A}}\left(2/\pi\right)^{3}\left[\sin^{-1}\left(\omega/\omega_{\mathrm{t}}\right)\right]^{2}}{Z\left(\omega_{\mathrm{t}}^{2}-\omega^{2}\right)^{1/2}}d\omega, \quad (1)$$

$$\omega_{\mathrm{t}} = v_{\mathrm{i}}K_{\max}\left(2/\pi\right), \quad (2)$$

where ω_{t} is the maximum frequency for each of the three acoustic modes at the zone boundary, $K_{\max}$ is the radius of the Brillouin zone, v_{i} is the sound velocity for each acoustic wave (longitudinal and shear waves), Z is the number of molecules in the unit cell (2 for stishovite), and N_A is Avogadro's number. The size of the Brillouin zone is given by,

$$K_{\max} = 2\pi\left(\frac{3N_{\mathrm{A}}}{4\pi ZV\mu}\right)^{1/3}, \quad (3)$$

where V is the specific volume and $\mu = 0.06008$ kg mol^{-1} of molecules.

The remaining vibrational degrees of freedom are treated as a continuum of optic modes, g_0, or individual Einstein oscillators, g_{E}. The vibrational density of states within the frequency range of the optic modes, $\omega_{\mathrm{l}} < \omega < \omega_{\mathrm{u}}$, and at the frequency of Einstein oscillators, ω_{E}, are given by,

$$g_0 = \frac{3N_{\mathrm{A}}n_{\mathrm{m}}\left[1-(1/s)-q_{\mathrm{E}}\right]}{\omega_{\mathrm{u}}-\omega_{\mathrm{l}}}, \quad (4)$$

$$g_{\mathrm{E}} = 3q_{\mathrm{E}}N_{\mathrm{A}}n_{\mathrm{m}}\delta\left(\omega-\omega_{\mathrm{E}}\right), \quad (5)$$

where n_{m} is the number of atoms per molecule, q_{E} is the proportion of optic modes stored in Einstein oscillators at frequency ω_{E}, and δ is the delta function.

The isochoric heat capacity, C_V, is determined by summing three functions that integrate over the density of states in the acoustic Λ, optical κ, and Einstein phonon modes ξ:

$$\Lambda\left(x_i\right) = \left(\frac{2}{\pi}\right)^{3}\int_{0}^{x_i}\frac{\left[\sin^{-1}\left(x/x_i\right)\right]^{2}x^{2}e^{x}}{\left(x_i^{2}-x^{2}\right)^{1/2}\left(e^{x}-1\right)^{2}}dx, \quad (6)$$

$$\kappa\left(\begin{array}{c} x_{\mathrm{u}} \\ x_{\mathrm{l}} \end{array}\right) = \int_{x_{\mathrm{l}}}^{x_{\mathrm{u}}}\frac{x^{2}e^{x}}{\left(x_{\mathrm{u}}^{2}-x_{\mathrm{l}}^{2}\right)^{1/2}\left(e^{x}-1\right)^{2}}dx, \quad (7)$$

$$\xi\left(x_E\right) = \frac{x_E^{2}e^{x_E}}{\left(e^{x_E}-1\right)^{2}}, \text{ and then} \quad (8)$$

$$C_V = \frac{3N_{\mathrm{A}}k_{\mathrm{B}}}{n_{\mathrm{m}}Z}\sum_{i=1}^{3}\Lambda\left(x_i\right)+3N_{\mathrm{A}}k_{\mathrm{B}}\left(1-\frac{3}{3n_{\mathrm{m}}Z}-q_{\mathrm{E}}\right)\kappa\left(\begin{array}{c} x_{\mathrm{u}} \\ x_{\mathrm{l}} \end{array}\right)$$

$$+3N_{\mathrm{A}}k_{\mathrm{B}}q_{\mathrm{E}}\xi\left(x_E\right), \tag{9}$$

where $x = \hbar\omega/k_{\mathrm{B}}T$.

To determine the isochoric heat capacity in the compressed state, Kieffer [1979] suggests integrating the definition of the mode Grüneisen parameter,

$$\gamma_{\mathrm{optic}} = -\frac{\partial \ln(\omega)}{\partial \ln(V)}, \tag{10}$$

to determine the change in frequency with volume of the optical modes. The wave velocity, v_{i}, for each acoustic mode is assumed to change according to [Kieffer, 1982],

$$v_{\mathrm{i}} = v_{0,\mathrm{i}}\left[1 - \left(\frac{V}{V_0} - 1\right)\left(\gamma_i - \frac{1}{3}\right)\right] \tag{11}$$

where V_0 is the volume of stishovite at ambient pressure, $v_{0,\mathrm{i}}$ is the ambient pressure sound velocity of acoustic mode i, and γ_i is the mode Grüneisen parameter of acoustic mode i. Then, the cutoff frequencies for each acoustic branch of the phonon spectrum can be calculated using Equations 2 and 3.

Next, we summarize the method discussed by Gillet et al. [1990], and references therein, to determine the effect of anharmonic potentials on the heat capacity. A mode anharmonic parameter a_i can be used to describe the anharmonicity of a vibrational mode of frequency ω_i,

$$a_i = \left(\frac{\partial \ln\omega_i}{\partial T}\right)_V. \tag{12}$$

The mode parameter, a_i, describes the change in frequency of a certain mode as a function of temperature at constant volume. As most experimental measurements are not performed at constant volume, but at constant pressure or temperature, it can be shown that

$$a_i = \alpha_T\left(\gamma_{iT} - \gamma_{iP}\right) \tag{13}$$

with

$$\gamma_{iT} = K\left(\frac{\partial \ln\omega_i}{\partial P}\right)_T, \tag{14}$$

$$\gamma_{iP} = -\frac{1}{\alpha_T}\left(\frac{\partial \ln\omega_i}{\partial T}\right)_P, \tag{15}$$

where α_T is the coefficient of thermal expansion and K is the bulk modulus.

To determine the effect of the anharmonicity parameter on the heat capacity of a material, we start with the internal energy, E, of a system of harmonic oscillators. The oscillator energy changes with temperature as

$$E(T) = k_{\mathrm{B}}T^2\left(\frac{\partial \ln Q}{\partial T}\right)_V. \tag{16}$$

Here Q is the partition function for a system of harmonic oscillators,

$$Q = \prod \frac{1}{1 - \exp\left(-\hbar\omega_i/k_{\mathrm{B}}T\right)}, \tag{17}$$

where the product is over all available vibrational modes of the system, ω_i.

Inserting Equation 17 into Equation 16, one obtains

$$E(T) = \sum E_i^h \left(1 - a_i T\right), \tag{18}$$

where E_i^h is the internal energy of harmonic oscillator i. The heat capacity at constant volume is then,

$$C_V = \sum \left[C_{Vi}^h \left(1 - a_i T\right) - a_i E_i^h\right], \tag{19}$$

where a_i is assumed to be independent of temperature. At high temperatures, E_i^h is approximately $C_{Vi}^h T$, where C_{Vi}^h is the isochoric heat capacity contribution from harmonic oscillator i. Consequently, Equation 19 can be further simplified to

$$C_V = \sum C_{Vi}^h \left(1 - 2a_i T\right). \tag{20}$$

The anharmonicity parameter, a_i, has been measured for a few optical modes of stishovite [Gillet et al., 1990]. However, as noted in Gillet et al. [1990], there is significant uncertainty in using the average of the anharmonicity parameters for the three measured vibrational modes. To constrain the anharmonicity parameter, we compare the measured shock temperature in the stishovite phase with a thermodynamic model for the shock temperature where the only unconstrained parameter is a_i.

For materials that undergo a high-pressure phase transition, shock temperatures are calculated using the method from Lyzenga and Ahrens [1980]. The internal energy increase of a material subjected to shock compression is determined by the Rankine-Hugoniot equation,

$$\Delta E = \frac{1}{2}\left(P_{\mathrm{H}} - P_{00}\right)\left(V_{00} - V_{\mathrm{H}}\right) \tag{21}$$

where subscript $_{00}$ denotes the pressure and volume of the starting phase. As the shocked state is in equilibrium, the calculation of internal energy is path independent. For a material shocked from a low-pressure phase to a high-pressure phase, such as fused quartz to stishovite, the internal energy increase upon going from the initial state (P_{00}, V_{00}) to the shock state (P_{H}, V_{H}) is obtained by summing the energy of transition from the low pressure to the high pressure phase E_{tr} (Table S.2) at P_{00}, the work done in compressing the the high-pressure phase isentropically from the initial volume V_0 to the volume in the shocked state V_{H}, and the energy of heating the material from the isentrope to the Hugoniot state:

$$\Delta E = E_{\mathrm{tr}} + \int_{V_0}^{V_{\mathrm{H}}} P_{\mathrm{S}} dV + \int_{T_{\mathrm{S}}}^{T_{\mathrm{H}}} C_V dT. \tag{22}$$

T_{S} is the temperature on the isentrope at volume V_{H}, and T_{H} is the temperature on the Hugoniot at volume V_{H}. We use a third-order Birch-Murnaghan EOS with parameters from Panero et al. [2003] to calculate pressure on the isentrope, $P_{\mathrm{S}}(V)$.

In spite of the large number of shock wave experiments performed on silica polymorphs, there are few accurate shock temperature measurements on silica that are confidently within the stishovite phase. Here we focus on the shock temperature measurement by Lyzenga et al. [1983] on silica glass shocked to stishovite [later corrected by Boslough,

1988]. At a shock pressure of 58.9±1 GPa, the shock temperature is 4960±100 K (where V_H=2.17(3)×10^{-4} m^3 kg^{-1} [Ahrens and Johnson, 1995]).

To match the measured shock temperature with the heat capacity model presented above (Equation 19) requires an average anharmonicity parameter of a_i=-3.1(6)×10^{-5} K^{-1}, which is slightly above the three measured anharmonicity parameters for individual optical modes of stishovite [Gillet et al., 1990]. The other parameters used in the Kieffer model calculation are given in Table S.3.

Using a_i=-3.1(6)×10^{-5} K^{-1}, the isochoric heat capacity of stishovite at a temperature of 4500 K is 3.65(0.15)k_B per atom, significantly above the Dulong-Petit limit. Note that we are forcing the phonon contribution to account for the entire temperature dependence of the entropy; however, at these high temperatures, it is not unlikely that transitions between electronic energy levels or defect generation may contribute to the heat capacity at high temperatures.

S2. Revised boiling point for SiO_2

S2.1. Heat capacity of liquid silica at 1 bar

The entropy change along an isobar is found by integrating the heat capacity at constant pressure, C_P, from T = 0 K, where the entropy is zero from the third law of thermodynamics, to the temperature of interest T^*,

$$S = \int_0^{T^*} \frac{C_P}{T} dT, \tag{23}$$

where C_P is defined below (Equation 24).

In the recent literature, there are two primary sources of data for C_P of silica liquid at 1 bar. The well-known JANAF thermodynamic tables are widely cited [Chase, 1998]; however, the heat capacity data above 1700 K are only estimates based upon extrapolation to lower temperature data by Wietzel [1921] and agreement with liquid heat capacities of various silicates. The second widely-cited source of heat capacity data for liquid silica is from Richet et al. [1982]. Where the enthalpy of silica glass was measured through the glass transition at ≈1600 K, for a fast cooling rate, up to 1776 K. The heat capacity data of Richet et al. [1982] are the most accurate measurements on silica liquid in the literature with error estimates of ∼0.3%. Note, however, that 1776 K is still below the equilibrium melting temperature of cristoballite, ∼1995 K. Using DFT-MD methods, Karki et al. [2007] found the isochoric heat capacity of liquid silica at 3000 K to be significantly higher than the measurements of Richet et al. [1982]. de Koker et al. [2008] re-analyzed the DFT-MD data of Karki et al. [2007] in a thermodynamically consistent manner and found the heat capacity to increase quasi-linearly from 3000 up to 6000 K; however, without any simulations below 3000 K, it is difficult to determine the source of the difference between the experimental data and the theoretical calculations. Recently, Ottonello et al. [2010] calculated the heat capacity of liquid silica up to 3000 K and found their calculated C_P to agree with heat capacity measurements of Richet et al. [1982]. de Koker (private communication) suggests the difference could be in the numerical models, the DFT-MD methods include depolymerization of the SiO_2 structure and the electronic contribution to the heat capacity, which would both cause an increase in the calculated heat capacity. However, it should be noted that DFT methods may underestimate the band gap and consequently overestimate the electronic contribution to the heat capacity.

Interestingly, there is more enthalpy data above 1800 K, from 1400 to 2400 K [Tarasov et al., 1973], that has been neglected in the literature due to scatter in the data. However, as the data is over a much larger temperature range than that of Richet et al. [1982], the enthalpy data were fit to a second order polynomial to obtain a temperature dependence to the isobaric heat capacity. Even with the reasonably high uncertainties in enthalpy, $0.8-1.3\%$, the combined data of Richet et al. [1982] and Tarasov et al. [1973] provide experimental constraints on the enthalpy and hence heat capacity over a wider temperature range than previously considered.

The best fit to the combined enthalpy data of Richet et al. [1982] and Tarasov et al. [1973] from 1600 to 2400 K is as follows,

$$C_P \text{ [J mol}^{-1}\text{K}^{-1}] = 80.1(1.8) + 0.0079(58)\,(T - 1600) \tag{24}$$

where temperature is in Kelvin and the covariance between the uncertainty in the intercept and the slope is -0.00465. Although the increase in heat capacity with temperature is relatively uncertain, it is significant. Since the band gap for SiO_2 is 8.9 eV [Laughlin, 1980], we expect the electronic contribution to the heat capacity to be small in the temperature range from 2000 to 3000 K.

S2.2. Entropy of liquid silica at 1 bar

Upon integration of all available thermodynamic data, Richet et al. [1982] calculated the absolute entropy of amorphous silica at the observed glass transition temperature of their experiments, S=154.757 J mol^{-1} K^{-1} at 1600 K. As the transition between glass and liquid is second order, there is no entropy discontinuity, and the heat capacity can be integrated across the glass transition temperature. Hence, above 1600 K, we use the isobaric heat capacity (Equation 24) to determine the entropy of liquid silica for temperatures above 1600 K:

$$\begin{aligned} S(T > 1600\text{K}) \;=\; & 154.0(3.0) + 80.1(1.8)\ln\left(\frac{T}{1600}\right) \\ & +0.0078(58)\left[(T - 1600) - 1600\ln\left(\frac{T}{1600}\right)\right]. \end{aligned} \tag{25}$$

We also calculated the enthalpy of liquid silica above 1600 K using the tabulated value from Richet et al. [1982] at 1600 K and the isobaric heat capacity (Equation 24), noting that the covariance between the uncertainty in the linear term and the quadratic term is -0.00465:

$$\begin{aligned} H(T > 1600\text{K}) - H(298\text{ K}) \;=\; & 87849 + 80.1(1.8)\,(T - 1600) \\ & +\frac{0.0079(58)}{2}\,(T - 1600)^2\,. \end{aligned} \tag{26}$$

S2.3. Equilibrium vaporization of silica

We include the following reactions to calculate equilibrium between liquid and vapor:

$$\text{SiO}_2^{(l)} \;\rightleftharpoons\; \text{SiO}^{(g)} + \frac{1}{2}\text{O}_2^{(g)}, \tag{27}$$

$$\frac{1}{2}\text{O}_2^{(g)} \;\rightleftharpoons\; \text{O}^{(g)}, \tag{28}$$

$$\text{SiO}_2^{(l)} \;\rightleftharpoons\; \text{SiO}_2^{(g)}. \tag{29}$$

Equilibrium between the reactions described in Equations 27 and 28 must be solved simultaneously with the constraint that the partial pressures of the product gases from reactions 27 to 29 must sum to 1 bar at the vaporization temperature. The equilibrium constants for reactions 27 and 28 are defined as follows,

$$K_{27} = \frac{P_{\mathrm{SiO}} P_{\mathrm{O_2}}^{1/2}}{a_{\mathrm{SiO_2}}} \tag{30}$$

$$K_{28} = \frac{P_{\mathrm{O}}}{P_{\mathrm{O_2}}^{1/2}} \tag{31}$$

$$K_{29} = \frac{P_{\mathrm{SiO_2}}}{a_{\mathrm{SiO_2}}} \tag{32}$$

where $a_{\mathrm{SiO_2}}$ is the activity of SiO_2 in the liquid phase. As in Schick [1960], we now make the assumption that the liquid is a pure compound and hence the activity of the pure phase is $a_{\mathrm{SiO_2}}$=1.

To calculate the equilibrium partial pressures within reactions 27 and 28, we assume a closed system. Thus, the number of moles, N, of molecular oxygen in the system can be related to the number of moles of SiO and atomic oxygen by

$$N_{\mathrm{O_2}} = \frac{1}{2} N_{\mathrm{SiO}} - \frac{1}{2} N_{\mathrm{O}}. \tag{33}$$

As 1 bar and a few thousand Kelvin is not close to the critical point for any of the species considered above, the ideal gas law is valid. Then, the relation between the partial pressures of the species is

$$P_{\mathrm{O_2}} = \frac{1}{2} P_{\mathrm{SiO}} - \frac{1}{2} P_{\mathrm{O}} \tag{34}$$

Equations 30 to 34 can be solved with knowledge of the equilibration constants or, more specifically, the difference in Gibbs free energy of reactions 27 to 29.

The Gibbs free energy of a reaction, ΔG_{rxn}, is most accurately determined from the heat of reaction less the entropy difference between the products and reactants, $\Delta H_{\mathrm{rxn}} - T\Delta S_{\mathrm{rxn}}$. The heat of formation of $SiO_2^{(l)}$, $\Delta^f H_{\mathrm{SiO_2^{(l)}}}$, was calculated at 2000 K by Richet et al. [1982]. As this calculation required only a small extrapolation of experimental calorimetry data, we expect the uncertainty to be similar to the uncertainty in the heat content data, $\sim 0.5\%$. There is a scarcity of information regarding the heat of formation of SiO gas; consequently, we consider the analysis by Schick [1960] of the heat of formation of SiO vapor at 2000 K to be reasonable. At $T = 2000$ K, the heats of formation are

$$\Delta^f H_{\mathrm{SiO_2^{(l)}}}\ (2000\ \mathrm{K}) = -934862 \pm 4674\ \ \mathrm{J\ mol^{-1}}, \tag{35}$$

$$\Delta^f H_{\mathrm{SiO^{(g)}}}\ (2000\ \mathrm{K}) = -151190 \pm 5289\ \ \mathrm{J\ mol^{-1}}. \tag{36}$$

The enthalpy change of reaction 27 at temperatures greater than 2000 K is then

$$\begin{aligned} \Delta H_{27}(T) = {} & \Delta^f H_{\mathrm{SiO^{(g)}}}(2000\ \mathrm{K}) \\ & + [H_{\mathrm{SiO^{(g)}}}(T) - H_{\mathrm{SiO^{(g)}}}(2000\ \mathrm{K})] \\ & + \frac{1}{2}\left[H_{\mathrm{O_2^{(g)}}}(T) - H_{\mathrm{O_2^{(g)}}}(2000\ \mathrm{K})\right] \end{aligned}$$

$$-\Delta^f H_{\mathrm{SiO}_2^{(l)}}(2000\ \mathrm{K}) - \left[H_{\mathrm{SiO}_2^{(l)}}(T) - H_{\mathrm{SiO}_2^{(l)}}(2000\ \mathrm{K})\right]. \quad (37)$$

The enthalpy of SiO_2 liquid above 2000 K is given in Equation 26. The enthalpy of O_2, tabulated in the JANAF thermochemical tables [Chase, 1998], was fit to a polynomial, which accurately describes the enthalpy of molecular oxygen as a function of temperature for T>2000 K:

$$H_{\mathrm{O}_2^{(g)}}(T) - H_{\mathrm{O}_2^{(g)}}(2000\ \mathrm{K}) = -63925 + 33.918T + 0.0009777T^2 \quad (38)$$

As uncertainties are not presented in the JANAF thermodynamic tables, we assume the same level of uncertainty in the enthalpy difference as presented in the analysis of Schick [1960], $\sim 1\%$.

The heat capacity of SiO vapor has not been measured. We assume the heat capacity follows the heat capacity of an ideal diatomic molecule at high temperatures, i.e. $C_P = \frac{9}{2}R$. Schick [1960] performed a more rigorous assessment of the enthalpy and entropy based on spectroscopic data; however, their rigorous derivation again suggests $C_P = \frac{9}{2}R$.

The entropy of reaction is just the difference in standard entropy at temperature T between products and reactants:

$$\Delta S_{27}(T) = S_{\mathrm{SiO}}(T) + \frac{1}{2}S_{\mathrm{O}_2}(T) - S_{\mathrm{SiO}_2}(T). \quad (39)$$

The entropy of SiO_2 liquid is given in Equation 25. The entropy of O_2 is obtained from the JANAF thermochemical table [Chase, 1998], where we fit the polynomial,

$$S_{\mathrm{O}_2^{(g)}}(T) = 211.5 + 0.0405T - 7.0794 \times 10^{-6}T^2 + 5.617 \times 10^{-10}T^3. \quad (40)$$

We defer to the calculation of the entropy of SiO gas by Schick [1960], where

$$S_{\mathrm{SiO}^{(g)}}(T) = 276.31 + \int_{2000}^{T} \frac{C_P}{T} dT, \quad (41)$$

and assume $C_P = \frac{9}{2}R$ over the temperature range of interest.

The enthalpy change of reaction 28 at temperatures above 2000 K is

$$\Delta H_{28}(T) = \Delta^f H_{\mathrm{O}^{(g)}}(2000\ \mathrm{K}) + [H_{\mathrm{O}^{(g)}}(T) - H_{\mathrm{O}^{(g)}}(2000\ \mathrm{K})] - \frac{1}{2}\left[H_{\mathrm{O}_2^{(g)}}(T) - H_{\mathrm{O}_2^{(g)}}(2000\ \mathrm{K})\right]. \quad (42)$$

The enthalpy and entropy of monatomic oxygen are tabulated in the JANAF thermodynamic tables and have been fit to a polynomial,

$$H_{\mathrm{O}^{(g)}}(T) - H_{\mathrm{O}^{(g)}}(2000\ \mathrm{K}) = -41188 + 20.404T + 9.4859 \times 10^{-5}T^2 \quad (43)$$

$$S_{\mathrm{O}^{(g)}}(T) = 168.04 + 0.024223T - 4.5631 \times 10^{-6}T^2 + 3.7315 \times 10^{-10}T^3 \quad (44)$$

and the heat of formation of monatomic oxygen at 2000 K is 255,299 J mol^{-1}.

The enthalpy change of reaction 29 at temperatures above 2000 K is

$$\begin{aligned}\Delta H_{29}(T) \;=\; & \Delta^f H_{\mathrm{SiO_2^{(g)}}}(2000\ \mathrm{K}) \\ & + \left[H_{\mathrm{SiO_2^{(g)}}}(T) - H_{\mathrm{SiO_2^{(g)}}}(2000\ \mathrm{K})\right] \qquad (45) \\ & -\Delta^f H_{\mathrm{SiO_2^{(l)}}}(2000\ \mathrm{K}) \\ & - \left[H_{\mathrm{SiO_2^{(l)}}}(T) - H_{\mathrm{SiO_2^{(l)}}}(2000\ \mathrm{K})\right]. \qquad (46)\end{aligned}$$

The enthalpy and entropy of SiO_2 gas, tabulated in the JANAF thermodynamic tables, were fitted with polynomials:

$$\begin{aligned} H_{\mathrm{SiO_2^{(g)}}}(T) - H_{\mathrm{SiO_2^{(g)}}}(2000\ \mathrm{K}) \;&=\; -121630 + 60.327T + 24.4\times10^{-5}T^2 \qquad (47) \\ S_{\mathrm{SiO_2^{(g)}}}(T) \;&=\; 237.13 + 0.069519T - 12.757\times10^{-6}T^2 \\ &\quad +10.178\times10^{-10}T^3 \qquad (48)\end{aligned}$$

and the heat of formation of SiO_2 gas at 2000 K is -361,747 J mol^{-1}.

Using the thermodynamic data detailed above, the Gibbs free energy of the reactions described in Equations 27 to 29 were fit with linear functions in temperature,

$$\begin{aligned}\Delta G_{27} \;&=\; 7.684\times10^5 - 231.7T, \qquad (49) \\ \Delta G_{28} \;&=\; 2.442\times10^5 - 61.57T, \qquad (50) \\ \Delta G_{29} \;&=\; 5.539\times10^5 - 153.3T, \qquad (51)\end{aligned}$$

where the free energy is in J mol^{-1} and temperature is in Kelvin. We find that the partial pressures of the vapor species in Equations 27 to 29 sum to 1 bar at 3177 K.

Due to the large, previously unknown, uncertainty in the heat capacity of SiO_2 liquid, the uncertainty in ΔG_{27} presented in Schick [1960] needs to be increased. As the uncertainty in the enthalpy and entropy are strongly correlated by the uncertainty in the heat capacity of the materials, to first order it is reasonable to approximate the uncertainty in the free energy of reaction with the uncertainty in the enthalpy of reaction. Using values for the uncertainty in the enthalpy of formation and heating of SiO gas and O_2 gas given in Schick [1960], the enthalpy of formation of SiO_2 liquid given in Richet et al. [1982], and the enthalpy of heating SiO_2 liquid determined here, we find the enthalpy of reaction 27 is uncertain to within ∼29,000 J mol^{-1} at 3000 K. Consequently, the boiling point will be uncertain to ±115 K.

S3. Streaked optical pyrometer calibration

The spectral radiance emitted from a surface at temperature T is described by Planck's law,

$$L(\lambda, T) = \epsilon \frac{2hc^2}{\lambda^5} \frac{1}{e^{hc/\lambda k_B T} - 1}, \qquad (52)$$

where ϵ is the emissivity, λ is the wavelength of light, and T is the temperature of the radiating surface. From Kirchoff's law for an opaque surface, ϵ=(1-R'), where R' is the frequency-dependent the reflectivity. Here we make the assumption that R' is frequency

independent over the range of interest. Based on previous measurements of spectrally resolved and absolutely calibrated detectors [Lyzenga et al., 1983], our assumption of gray-body emission is reasonable. For a pyrometer that collects light over a small wavelength band, Planck's law can be inverted into a form more suitable for apparent temperature measurements,

$$T_{\mathrm{a}} = \frac{T_0}{\ln\left(1 + \frac{A}{I_{\mathrm{cor}}}\right)}, \tag{53}$$

where T_0 and A are coefficients determined from calibration of the pyrometer and I_{cor} is the pyrometer signal corrected for a non-zero reflectivity [Celliers et al., 2010].

In Figure S.2, the spectral response of the Janus Streaked Optical Pyrometer (SOP) is given as a function of wavelength (which includes transmission through the optical components and wavelength dependence of the Hamamatsu C7700 streak camera detector efficiency). Quartz shock temperatures were absolutely calibrated using the SOP at the Omega laser, which has a sensitivity spectrum similar to Figure S.2. However, the spectrum is split into two channels at Omega, and consequently, it is reasonable to treat the emission from each channel as though it occurs over a small wavelength range [Miller et al., 2007]. At Janus, radiation from the entire spectrum (Figure S.2) is combined into one channel; hence, a delta function approximation for the emitting frequency does not seem appropriate.

However, upon simulating the combined thermal emission with the SOP response (Figure S.3), we find the error in using Equation 53 to be less than 2% over the temperature range of interest here. At temperatures greater than 20,000 K, the error in using Equation 53 can increase beyond 5% and should be accounted for in data analysis of high-temperature shock wave experiments.

We fit the SOP calibration coefficients T_0 and A to shock velocity–I_{cor} data from six different experiments (with no intermediate modifications to the SOP or collecting optics). The structure in the thermal emission from quasi-steady shock waves is similar to the structure in the shock velocity measurements. Paired intensity and shock velocity data were selected at locations with correlated structure for the calibration, as shown in Figure S.4. The paired shock velocity and intensity data were taken at least 2 ns after the shock wave enters the quartz to avoid any possible pre-heating related to hard x-ray deposition within the quartz sample. The intensity of the thermal emission is corrected for the reflectivity of the shock front using the reflectivity of quartz as a function of shock velocity [Celliers et al., 2010]. For targets that did not have an anti-reflective coating on the downrange free surface, a second correction for the reflectivity of an interface between disparate indices of refraction was done using the Fresnel equation (1.547 for c-axis quartz). The calibration uses the shock velocity–temperature calibration from Hicks et al. [2006] with the corrected reflectivity from Celliers et al. [2010]. The fit to Equation 53 is shown in Figure S.5. The least-squares fitted coefficients are $A = 3140(760)$ [counts] and $T_0 = 24300(2350)$ [K] with a covariance of 1.745×10^6.

For the lowest-pressure experiment (e100727s1 in Figure S.5), the SOP intensity data were not determined from the companion shock wave velocities because of the lack of reflectivity in the shock front. Instead, the intensity is calibrated by the superheating signature in quartz. As superheating temperatures are rate dependent [Luo et al., 2003b],

we calibrate using the temperature measurements of Hicks et al. [2006] rather than the more accurate gas-gun measurements by Lyzenga et al. [1983].

Upon formal propagation of errors, the uncertainty in the post-shock temperature measurements is $\sim 11\%$, which is a combination of both the uncertainty in the fit presented in Figure S.5 and the 8% uncertainty in calibration of the quartz standard by Hicks et al. [2006]. The uncertainty in our calibration fit is due to random noise and spatial variability in the SOP ($> 5\%$) and the random error in shock velocity measurement ($2\% - 4\%$). The uncertainty in the reflectivity correction to $I_{\rm cor}$ is small due to the low reflectivity at these pressures.

S4. Absorbance of silica fluid

We used first-principle MD simulations to generate samples of thermally perturbed positions for a model of fluid silica with 96 atoms under temperature and pressures relevant to planetary impacts. In FPMD, the forces governing the dynamics are evaluated using Density Functional Theory (DFT) [Hohenberg and Kohn, 1964], which is in principle an exact representation of the many-body Schrödinger equation and in practice is only limited by the approximation of the exchange-correlation functional. The FPMD simulations were performed using the Vienna ab initio Simulation Package (VASP) [Kresse and Hafner, 1993]. We used the Perdew-Burke-Ernzerhof (PBE) [Perdew et al., 1996] level of approximation to the exchange correlation functional with projector-augmented wave (PAW) [Blochl, 1994] pseudopotentials to account for the core electrons. We used Born-Oppenheimer MD (BOMD) within the NVT-ensemble (with a Nose-Hoover thermostat with a frequency of 13.2 THz and a 1.0 fs ionic time step). For the MD, the Brillouin zone was sampled at the Γ-point and the plane-wave cutoff was set to 1200 eV. The electron occupancy are set according to a Fermi-Dirac distribution function ($T_e = T_{ions}$). For the optical properties post-processing calculations, the sample configurations are drawn from a 5 ps trajectory (after equilibration). We used 30 well spaced configurations, a lower plane-wave cutoff of 900 eV, a smearing of 0.03 eV for the spectra and enough unoccupied bands to cover all excitations within a 80 eV window. For each configuration drawn from the trajectories, we used the Gamma point electronic density from the MD to evaluate the set of Kohn-Sham orbitals at the $(\frac{1}{4}, \frac{1}{4}, \frac{1}{4})$ k-point (again using Fermi broadening at the ionic temperature). Based on these orbitals, we use the Kubo-Greenwood formula to estimate the real component of the frequency dependent conductivity, $\sigma_1(\omega)$ [e.g. Mattsson and Desjarlais, 2006; Holst et al., 2008]. The DC conductivity is obtained as the zero frequency limit of $\sigma_1(\omega)$ averaged over the different configurations while the imaginary component of the conductivity is obtained using the Kramers-Kronig transform. Using the complex conductivity, we can get the complex dielectric function, the index of refraction, and the coefficient of extinction. To get an estimate of the opacity of the vapor, we ran a short MD simulation using 4 SiO molecules and 2 O_2 molecules in a large volume to capture a sample of bond vibrations. The density was 0.0092 g/cc. Here, a plane-wave cutoff of 500 eV was used. Configurations from this short MD were used to get the conductivity with enough unoccupied bands to cover all excitations within a 11 eV window.

The FPMD-DFT opacity calculations are thought to be reasonably accurate for silicate fluids based on their previous success in predicting optical properties of supercritical

fluids [Laudernet et al., 2004; Clérouin et al., 2005]. Given the computational expense in calculating the opacity at a single (ρ,T) point, creating a opacity table from DFT calculations that is sufficiently populated for accurate interpolation is not yet feasible.

Hence, we use a semiconductor type Drude model to determine how the opacity scales as a function of density and temperature. The Drude model has been shown to adequately describe the increase in reflectivity along the supercritical fluid Hugoniot of LiF, Al_2O_3, H_2O, and He [Hicks et al., 2003; Celliers et al., 2004, 2010]. We use the FPMD-DFT calculations to constrain the parameters in the Drude model.

The Drude model for the conductivity is given as,

$$\sigma(\omega) = \frac{n_{\rm e} e_{\rm c}^2 \tau_{\rm e}}{2\epsilon_0 m_{\rm eff}(1 - i\omega\tau_{\rm e})}, \tag{54}$$

where $n_{\rm e}$ is the free electron concentration, $e_{\rm c}$ is the charge on the electron, $\tau_{\rm e}$ is the electron relaxation time, $m_{\rm eff}$ is the effective mass of the electron, which is approximately the mass of an electron, and ω is the angular frequency. For disordered materials the electron relaxation time $\tau_{\rm e}$ is close to the Ioffe-Regel limit [Ioffe and Regel, 1960], at which the scattering length is close to the interatomic distance R_0. The relaxation time is then $\tau_{\rm e} = R_0/u_{\rm e}$, where $u_{\rm e}$ is the mean electron velocity, which is approximately proportional to $T^{1/2}$; consequently $\tau_{\rm e} = A_0\rho^{1/3}T^{-1/2}$, where A_0 is a constant. The free electron concentration $n_{\rm e}$ in the semiconductor model is described by the carrier concentration of an intrinsic semiconductor [Kittel and Kroemer, 1980], which for thermal energies lower than the gap energy scales approximately as

$$n_{\rm e} = n_0 T^{3/2} \exp\left(-\frac{E_{\rm g}(\rho, T)}{2k_{\rm B}T}\right), \tag{55}$$

where $E_{\rm g}$ is the gap energy and n_0 is a constant. The gap energy has been found to be linearly dependent on density and temperature for a number of materials [Hicks et al., 2003; Celliers et al., 2004, 2010], and consequently, we assume the form below for SiO_2 in the expanded regime,

$$E_g = A_1 + A_2\rho + A_3 T, \tag{56}$$

where A_1, A_2, and A_3 are constants.

The frequency-dependent absorption coefficient $\alpha(\omega)$ is given by [Clérouin et al., 2005]

$$\alpha(\omega) = \frac{4\pi\sigma_1(\omega)}{n_1(\omega)c}, \tag{57}$$

where c is the speed of light and $n_1(\omega)$ is the real part of the index of refraction. As $n_1(\omega)$ has a relatively weak dependence on temperature and density, we consider it a constant.

Substituting the previously mentioned scalings for $\tau_{\rm e}$, $n_{\rm e}$, and the real part of the conductivity $\sigma'(\omega)$, one finds

$$\alpha(\omega) = \frac{4\pi}{n_1 c}\frac{e_c^2}{2m_e\epsilon_0}\frac{A_0\rho^{1/3}T^{-1/2}}{(1+\omega^2\tau_{\rm e})} n_0 T^{3/2} e^{-\frac{A_1+A_2\rho+A_3T}{k_BT}}. \tag{58}$$

As the electron relaxation time $\tau_{\rm e}$, is greater than ω when the mean electron velocity is comparable to the Fermi velocity of metals, we assume $\omega^2\tau_{\rm e}^2 \ll 1$. Note that this

assumption also removes any frequency dependence of the absorbance. Collecting terms that are independent of of temperature and density, and normalizing the temperature and density terms by arbitrary constants T_n and ρ_n, we find the absorption coefficient scales as,

$$\alpha_{\rm vap} = B_0 \left(\frac{\rho}{\rho_n}\right)^{1/3} \left(\frac{T}{T_n}\right) \mathrm{e}^{-B_1 \frac{T_n}{T}} \mathrm{e}^{-B_2 \frac{\rho T_n}{\rho_n T}}, \tag{59}$$

where B_1 and B_2 are dimensionless fitting parameters and B_0 scales the absolute absorbance and has units of absorbance.

To compare with the FPMD-DFT calculations of frequency dependent absorbance, we calculate a Rosseland mean absorption coefficient $\alpha_{\rm RM}$ for each DFT point,

$$\frac{1}{\alpha_{RM}} = \frac{\int_0^\infty \frac{\kappa_\lambda}{\alpha(\lambda)} \frac{\partial L_\lambda}{\partial T} d\lambda}{\int_0^\infty \kappa_\lambda \frac{\partial L_\lambda}{\partial T} d\lambda} \tag{60}$$

where the weighting function κ_λ describes the spectral response of the SOP and L_λ is the Planck function. The mean absorption coefficient ranges from 0.008 mm^{-1} for the silicate vapor at $\sim$ 9 kg m^{-1} and 4150 K up to 4400 mm^{-1} for the silicate liquid at 1900 kg m^{-1} and 4150 K.

To constrain B_0, B_1, and B_2, we fit Equation 59 to the mean absorption coefficients calculated using Equation 60. Using ρ_n = 1900 kg m^{-1} and T_n = 4150 K, we find $B_0 = 6.0 \times 10^{14}$ [mm^{-1}], $B_1 = 37$, $B_2 = -11.6$. The fit is shown in Figure S.6.

Spectroscopic measurements of post-shock thermal emission from samples of diopside shocked into the high pressure fluid phase suggest that the vapor phase could be partially ionized [e.g. Kurosawa et al., 2012]. However, in their measurements the shock state in the diopside was not measured and so it is not clear that the measurements are in a comparable region of the phase diagram.

Ionization is not taken into account in our radiative transfer model because the ionization energies for silicon and oxygen are sufficiently high to expect negligible vaporization at the measured temperatures in these experiments. More work is needed to determine the quantitative effect of ionization on the thermodynamics of shock induced vaporization.

References

Ahrens, T. J., Johnson, M. L., 1995. Shock wave data for minerals. In: Ahrens, T. J. (Ed.), Mineral Physics and Crystallography, A Handbook of Physical Constants, Vol. 2. American Geophysical Union, Washington, D. C., pp. 143–184.

Akaogi, M., Yusa, H., Shiraishi, K., Suzuki, T., 1995. Thermodynamic properties of α-quartz, coesite, and stishovite and equilibrium phase relations at high pressures and high temperatures. Journal of Geophysical Research 100 (B11), 22337–22347, doi:10.1029/95JB02395.

Akins, J. A., Ahrens, T. J., 2002. Dynamic compression of SiO_2: A new interpretation. Geophysical Research Letters 29 (10), 31, doi:10.1029/2002GL014806.

Blochl, P. E., 1994. Projector augmented-wave method. Physical Review B 54, 17953–17979, doi:10.1103/PhysRevB.50.17953.

Boslough, M. B., 1988. Postshock temperatures in silica. Journal of Geophysical Research 93 (B6), 6477–6484, doi:10.1029/JB093iB06p06477.

Celliers, P. M., Collins, G. W., Hicks, D. G., Koenig, M., Henry, E., Benuzzi-Mounaix, A., Batani, D., Bradley, D. K., Da Silva, L. B., Wallace, R. J., Moon, S. J., Eggert, J. H., Lee, K. K. M., Benedetti, L. R., Jeanloz, R., Masclet, I., Dague, N., Marchet, B., Le Gloahec, M. R., Reverdin, C., Pasley, J., Willi, O., Neely, D., Danson, C., 2004. Electronic conduction in shock-compressed water. Physics of Plasmas 11 (8), L41–L44, doi:10.1063/1.1758944.

Celliers, P. M., Loubeyre, P., Eggert, J. H., Brygoo, S., McWilliams, R. S., Hicks, D. G., Boehly, T. R., Jeanloz, R., Collins, G. W., 2010. Insulator-to-conducting transition in dense fluid helium. Physical Review Letters 104 (18), 184503, doi:10.1103/PhysRevLett.104.184503.

Chase, M. W., 1998. NIST-JANAF thermochemical tables. Monograph No. 9. American Institute of Physics, Washington, DC.

Clérouin, J., Laudernet, Y., Recoules, V., Mazevet, S., 2005. Ab initio study of the optical properties of shocked LiF. Physical Review B 72, 155122, doi:10.1103/PhysRevB.72.155122.

de Koker, N., Stixrude, L., Karki, B. B., 2008. Thermodynamics, structure, dynamics, and freezing of Mg_2SiO_4 liquid at high pressure. Geochimica et Cosmochimica Acta 72, 1427–1441, doi:10.1016/j.gca.2007.12.01.

Gillet, P., Lecleach, A., Madon, M., 1990. High-temperature Raman-spectroscopy of SiO_2 and GeO_2 polymorphs: Anharmonicity and thermodynamic properties at high-temperatures. Journal of Geophysical Research 95 (B13), 21635–21655, doi:10.1029/JB095iB13p21635.

Hicks, D. G., Boehly, T. R., Eggert, J. H., Miller, J. E., Celliers, P. M., Collins, G. W., 2006. Dissociation of liquid silica at high pressures and temperatures. Physical Review Letters 97 (2), 025502, doi:10.1103/PhysRevLett.97.025502.

Hicks, D. G., Celliers, P. M., Collins, G. W., Eggert, J. H., Moon, S. J., 2003. Shock-induced transformation of Al_2O_3 and LiF into semiconducting liquids. Physical Review Letters 91 (3), 035502, doi:10.1103/PhysRevLett.91.035502.

Hohenberg, P., Kohn, W., 1964. Inhomogeneous electron gas. Physical Review B 136 (3B), B864, doi:10.1103/PhysRev.136.B864.

Holst, B., Redmer, R., Desjarlais, M. P., 2008. Thermophysical properties of warm dense hydrogen using quantum molecular dynamics simulations. Physical Review B 77 (18), doi:10.1103/PhysRevB.77.184201.

Ioffe, A. F., Regel, A. R., 1960. In: Gibson, A. F., Kroger, F. A., Burgess, R. E. (Eds.), Progress in Semiconductors. Vol. 4. John Wiley and Sons, New York, p. 237.

Karki, B. B., Bhattarai, D., Stixrude, L., 2007. First-principles simulations of liquid silica: Structural and dynamical behavior at high pressure. Physical Review B 76 (10), doi:10.1103/PhysRevB.76.104205.

Kieffer, S. W., 1979. Thermodynamics and lattice-vibrations of minerals: 3. Lattice-dynamics and an approximation for minerals with application to simple substances and framework silicates. Reviews of Geophysics 17 (1), 35–59, doi:10.1029/RG017i001p00035.

Kieffer, S. W., 1982. Thermodynamics and lattice-vibrations of minerals: 5. Applications to phase-equilibria, isotopic fractionation, and high-pressure thermodynamic properties. Reviews of Geophysics 20 (4), 827–849, doi:10.1029/RG020i004p00827.

Kittel, C., Kroemer, H., 1980. Thermal Physics. W. H. Freeman and Company, New York.

Knudson, M., Desjarlais, M., 2009. Shock compression of quartz to 1.6 TPa: Redefining a pressure standard. Phys. Rev. Lett. 103, 225501, doi:10.1103/PhysRevLett.103.225501.

Kresse, G., Hafner, J., 1993. AB-initio molecular-dynamics for liquid-metals. Physical Review B 47 (1), 558–561, doi:10.1103/PhysRevB.47.558.

Kurosawa, K., Kadono, T., Sugita, S., Shigemori, K., Sakaiya, T., Hironaka, Y., Ozaki, N., Shiroshita, A., Cho, Y., Tachibana, S., Vinci, T., Ohno, S., Kodama, R., Matsui, T., 2012. Shock-induced silicate vaporization: The role of electrons. Journal of Geophysical Research-Planets 117, E04007, DOI10.1029/2011JE004031.

Laudernet, Y., Clérouin, J., Mazevet, S., 2004. Ab initio simulations of the electrical and optical properties of shock-compressed SiO_2. Physical Review B 72, 155122, doi:10.1103/PhysRevB.70.165108.

Laughlin, R. B., 1980. Optical absorption edge of SiO_2. Physical Review B 22 (6), 3021–3029, doi:10.1103/PhysRevB.22.3021.

Luo, S. N., Ahrens, T. J., Asimow, P. D., 2003a. Polymorphism, superheating, and amorphization of silica upon shock wave loading and release. Journal of Geophysical Research 108 (B9), 2421, doi:10.1029/2002JB002317.

Luo, S. N., Ahrens, T. J., Cagin, T., Strachan, A., Goddard, W. A., Swift, D. C., 2003b. Maximum superheating and undercooling: Systematics, molecular dynamics simulations, and dynamic experiments. Physical Review B 68, 134206, doi:10.1103/PhysRevB.68.134206.

Lyzenga, G. A., Ahrens, T. J., 1980. Shock temperature measurements in Mg_2SiO_4 and SiO_2 at high pressures. Geophysical Research Letters 7 (2), 141–144, doi:10.1029/GL007i002p00141.

Lyzenga, G. A., Ahrens, T. J., Mitchell, A. C., 1983. Shock temperatures of SiO_2 and their geophysical implications. Journal of Geophysical Research 88 (B3), 2431–2444, doi:10.1029/JB088iB03p02431.

Mattsson, T. R., Desjarlais, M. P., 2006. Phase diagram and electrical conductivity of high energy-density water from density functional theory. Physical Review Letters 97 (1), doi:10.1103/PhysRevLett.97.017801.

McQueen, R. G., 1992. The velocity of sound behind strong shocks in SiO_2. In: Schmidt, S., Dick, R. D., Forbes, J., Tasker, D. G. (Eds.), Shock Compression of Condensed Matter - 1991. Elsevier Science Publishers, Amsterdam, pp. 75–78.

Melosh, H. J., 2007. A hydrocode equation of state for SiO_2. Meteoritics & Planetary Science 42 (12), 2079–2098, doi:10.1111/j.1945-5100.2007.tb01009.x.

Miller, J. E., Boehly, T. R., Melchior, A., Meyerhofer, D. D., Celliers, P. M., Eggert, J. H., Hicks, D. G., Sorce, C. M., Oertel, J. A., Emmel, P. M., 2007. Streaked optical pyrometer system for laser-driven shock-wave experiments on OMEGA. Review of Scientific Instruments 78 (3), 034903, doi:10.1063/1.2712189.

Navrotsky, A., 1995. Energetics of silicate melts. Reviews in Mineralogy 32, 121–143.

Ottonello, G., Zuccolini, M. V., Belmonte, D., 2010. The vibrational behavior of silica clusters at the glass transition: Ab initio calculations and thermodynamic implications. Journal of Chemical Physics 133 (10), 104508, doi:10.1063/1.3483195.

Panero, W. R., Benedetti, L. R., Jeanloz, R., 2003. Equation of state of stishovite and interpretation of SiO_2 shock-compression data. Journal of Geophysical Research 108 (B1), 2015, doi:10.1063/1.2712189.

Perdew, J. P., Burke, K., Ernzerhof, M., 1996. Generalized gradient approximation made simple. Physical Review Letters 77 (18), 3865–3868, doi:10.1103/PhysRevLett.77.3865.

Richet, P., Bottinga, Y., 1986. Thermochemical properties of silicate glasses and liquids: A review. Reviews of Geophysics 24 (1), 1–25, doi:10.1029/RG024i001p00001.

Richet, P., Bottinga, Y., Denielou, L., Petitet, J., 1982. Thermodynamic properties of quartz, cristobalite and amorphous SiO_2: drop calorimetry measurements between 1000 and 1800 K and a review from 0 to 2000 K. Geochemica et Cosmochimica Acta 46, 2639–2658, doi:10.1016/0016-7037(82)90383-0.

Robie, R. A., Hemingway, B. S., Fisher, J. R., 1978. Thermodynamic Properties of Minerals and Related Substances at 298.15 K and 1 Bar (10^5 Pascals) Pressure and at Higher Temperatures. U.S. Geological Survey Bulletin 1452. U.S. Government Printing Office, Washington, DC.

Robie, R. A., Waldbaum, D. R., 1968. Thermodynamic properties of minerals and related substances at 298.15 K (25.0 C) and one atmosphere (1.013 Bars) pressure and at higher temperatures. U.S. Geological Survey Bulletin 1259. U.S. Government Printing Office, Washington, DC.

Saxena, S., Chatterjee, Y., Fei, Y., Shen, G., 1993. Thermodynamic Data on Oxides and Silicates. Springer Verlag, New York.

Schick, H. L., 1960. A thermodynamic analysis of the high-temperature vaporization properties of silica. Chemical Reviews 60 (4), 331–362, doi:10.1021/cr60206a002.

Tarasov, V. D., Chekhovskoi, V. Y., Puchkova, G. A., 1973. Enthalpy of several grades of quartz glass within the 1300-2450 °K temperature range. Journal of Engineering Physics and Thermophysics 25 (2), 1054–1056, doi:10.1007/BF00829860 (Translated from Inzhenerno-Fizicheskii Zhurnal 25 (2), 341-344, 1973.).

Trunin, R. F., 1994. Shock compressibility of condensed materials in strong shock waves generated by underground nuclear explosions. Physics-Uspekhi 37 (11), 1123–1145, doi:10.1070/PU1994v037n11ABEH000055.

Trunin, R. F., 1998. Shock Compression of Condensed Materials. Cambridge University Press, Cambridge.

Weidner, D. J., Bass, J. D., Ringwood, A. E., Sinclair, W., 1982. The single-crystal elastic moduli of stishovite. Journal of Geophysical Research 87 (B6), 4740–4746, doi:10.1029/JB087iB06p04740.

Wietzel, R., 1921. Die stabilitätsverhältnisse der glas- und kristallphase des siliziumdioxydes. Zeitschrift für anorganische und allgemeine Chemie 116 (1), 71–95, doi:10.1002/zaac.19211160108.

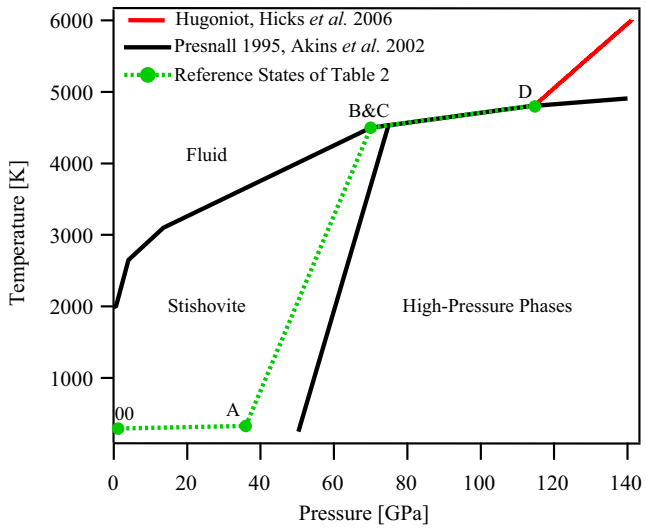

Figure S.1. Reference entropy states of Table 2 plotted on a pressure-temperature phase diagram of silica. The stability region of stishovite is expanded beyond that of the equilibrium phase diagram to represent the zero pressure reference state used in the main text.

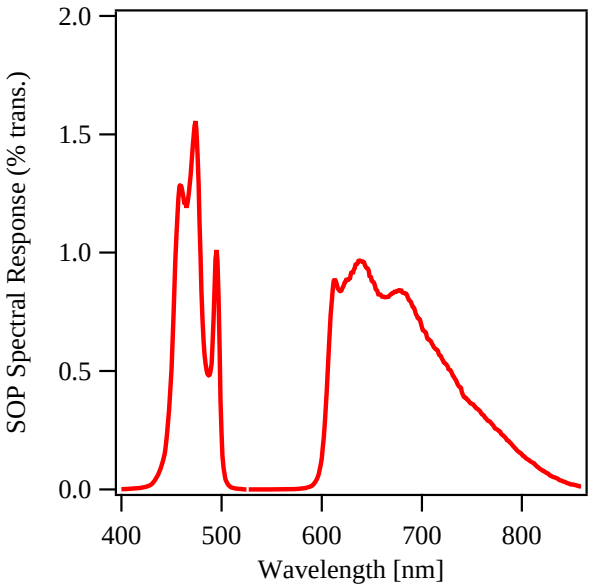

Figure S.2. Spectral response of the streaked optical pyrometer used in post-shock temperature measurements at the Janus laser. The gap in transmission from 500 to 600 nm was created by multiple notch filters used to block light from the drive laser (527 nm) and the VISAR probe laser (532 nm).

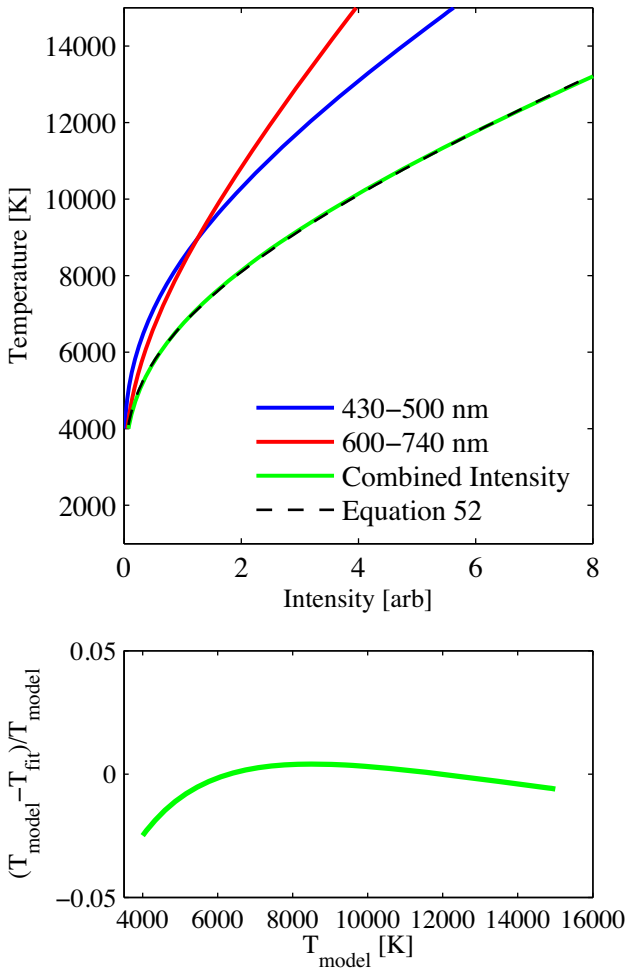

Figure S.3. Top: Model streaked optical pyrometer intensity as a function of temperature for emission bands from 430–500 nm (blue), 600–740 nm (red), and the combined emission spectrum (green). Equation 53 is fit to the combined spectrum (dashed black line). Bottom: Relative difference between the model temperature and the temperature derived from Equation 53. The error is less than 2% for the range of temperatures considered here.

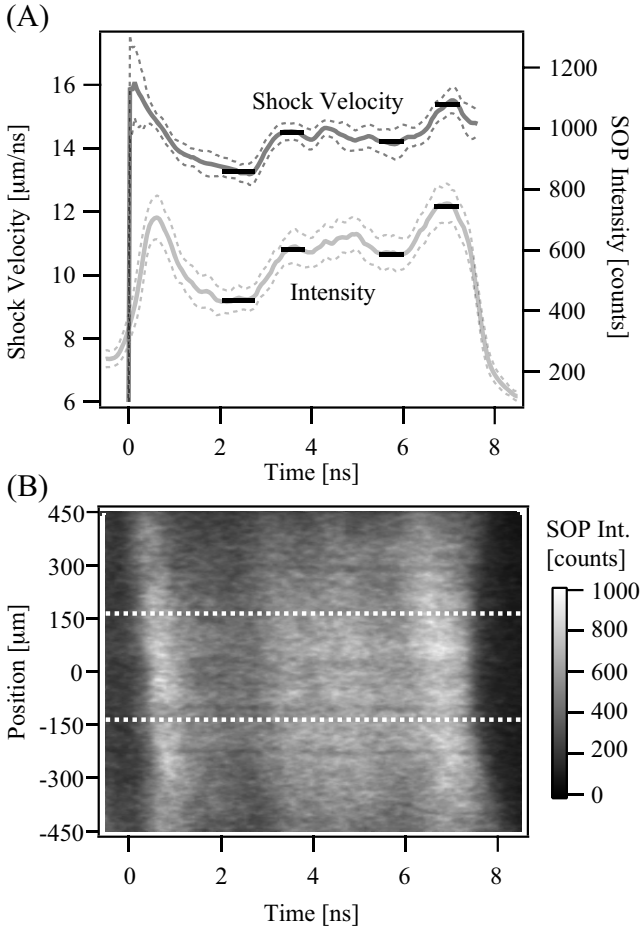

Figure S.4. (A) Shock velocity and corrected streaked optical pyrometer (SOP) intensity I_{cor} from shot e100726s4. The dark grey line (dashed) represents the shock velocity (uncertainty), light grey line (dashed) represents the corrected thermal emission (uncertainties) measured by the SOP for the same experiment. Dark horizontal bars represent regions of time where we are confident the shock velocity corresponds to the respective SOP intensity (i.e., where the structure in the profiles are obviously corresponding). (B) SOP image from shot e100726s4, dashed white lines represent region of space over which the corrected SOP intensity was taken. Uncertainties from part (A) of this figure are determined from the scatter in the SOP intensity at a given time. For the given laser spot size and target thickness, lateral release waves do not reach the area of interest.

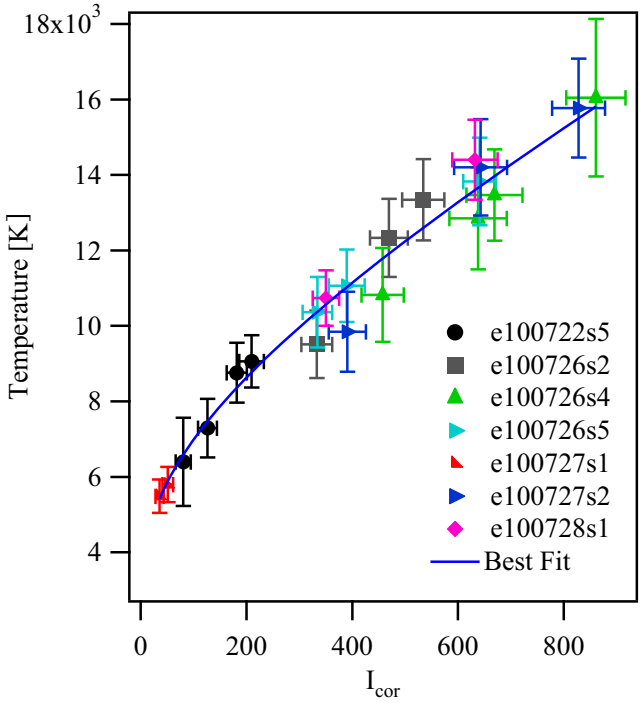

Figure S.5. Streaked optical pyrometer calibration. Data from individual experiments (symbols) are fit to Equation 53. The least-squares fitted coefficients are $A = 3140(760)$ [counts] and $T_0 = 24300(2350)$ [K] with a covariance of 1.745×10^6.

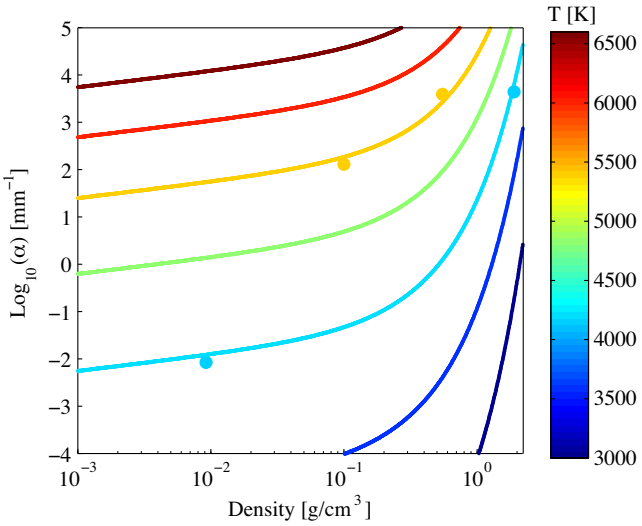

Figure S.6. Comparison of DFT-MD absorbance calculations for silica over a range of temperatures and densities (filled circles), with fitted absorbance model (lines, Equation 59) based on semiconducting Drude model.

Table S.1. Summary of variables and annotations used in the Auxiliary Materials.

Symbol	Definition
General Variables	
P	Pressure
V	Specific volume
E	Internal energy
T	Temperature
S	Entropy
H	Enthalpy
ω	Angular frequency
$h, \hbar$	Planck constant, reduced Planck constant
c	Speed of light
k_B	Boltzmann constant
N_A	Avogadro's number
R	Gas constant
$_\mathrm{H}$	Subscript denoting state on the Hugoniot
$_{00}$	Subscript denoting initial state on the Hugoniot
$_\mathrm{S}$	Subscript denoting state on an isentrope
Heat capacity of stishovite (§S1)	
$g(\omega)$	Vibrational density of states
ω_t	Maximum frequency of acoustic vibrational modes at zone boundaries
K_max	Radius of the Brillouin zone
Z	Number of SiO_2 molecules in unit cell
μ	Molar mass
g_0	Frequency continuum of optic modes
v_i	Sound velocity of each acoustic mode
n_m	Number of atoms per molecule
q_E	Proportion of optic modes stored in Einstein oscillators
$\omega_\mathrm{l}, \omega_\mathrm{u}$	Lower and upper frequency bounds to continuum of optic modes
ω_E	Frequency of Einstein oscillators
C_V	Isochoric heat capacity
Λ, κ, ξ	Density of state functions for acoustic, optical, and Einstein phonon modes, respectively
x	$\hbar\omega/k_\mathrm{B}T$
γ_i	Mode Grüneisen parameter for acoustic mode i
V_0	Specific volume of stishovite at ambient pressure
$v_{0,\mathrm{i}}$	Ambient pressure sound velocity of acoustic mode i
a_i	Linear anharmonicity parameter
α_T	Coefficient of thermal expansion
K	Adiabatic bulk modulus
Q	Partition function for a system of harmonic oscillators
E_i^h	Internal energy of harmonic oscillator i
C_{Vi}^h	Contribution to the isochoric specific heat from harmonic oscillator i
E_tr	Specific energy of transformation from low to high pressure phase

Table S.1. Summary of variables and annotations used in the Auxiliary Materials (continued).

Symbol	Definition
Revised boiling point for SiO_2 (§S2)	
$^{(g)}$	Superscript denoting gas phase
$^{(l)}$	Superscript denoting liquid phase
C_P	Isobaric heat capacity
$K_{\mathrm{Eq.i}}$	Equilibrium constant for reaction i
$\Delta^f H$	Heat of formation
N	Number of moles
G	Gibbs free energy
Streaked optical pyrometer (SOP) calibration (§S3)	
L	Radiance
ϵ	Emissivity
λ	Wavelength
R'	Frequency-dependent optical reflectivity
T_0, A	Calibration coefficients (Equation 53)
I_{cor}	Reflectivity-corrected SOP intensity
Absorbance of silica fluid (§S4)	
σ	Frequency-dependent conductivity
n_{e}	Free electron concentration
e_{c}	Charge of an electron
τ_{e}	Electron relaxation time
ϵ_0	Permittivity of free space
m_{eff}	Effective electron mass
R_0	Interatomic distance
u_{e}	Mean electron velocity
E_{g}	Band gap energy
A_0, A_1, A_2	Constants for linearized E_{g} (Equation 56)
T_n, ρ_n	Normalization constants (Equation 59)
B_0, B_1, B_2	Fitting parameters (Equation 59)
$\alpha(\omega)$	Frequency-dependent absorption coefficient
$n_1(\omega)$	Real part of the frequency-dependent index of refraction
σ_1	Real part of frequency-dependent conductivity
α_{vap}	Absorption coefficient along the release isentrope
α_{RM}	Rosseland mean absorption coefficient
κ_λ	Spectral response of the Streaked Optical Pyrometer
L_λ	Planck function

Table S.2. Published enthalpies of transition for quartz to stishovite and fused quartz to stishovite.

Source	ΔH [MJ kg^{-1}] quartz to stishovite	ΔH [MJ kg^{-1}] fused quartz to stishovite
Panero et al. [2003][a]	0.89	0.70
Lyzenga et al. [1983][b]	0.822	0.697
Akins and Ahrens [2002][c]	0.86	0.70
Luo et al. [2003a][d]	0.7772	–
Akaogi et al. [1995][e]	0.6162	0.464

The primary sources of the thermodynamic data are: (a) Robie and Waldbaum [1968], (b) Robie et al. [1978], (c) Navrotsky [1995] and Richet and Bottinga [1986] (d) Saxena et al. [1993], (e) our recommended value used in calculating the stishovite Hugoniot, transition enthalpy from fused quartz to stishovite determined using enthalpy data for fused quartz from Richet et al. [1982] (heat of formation of quartz at 298 K is 910.700 kJ mol^{-1}, heat of formation of fused quartz at 298 K is 901.554 kJ mol^{-1}, at 0.06008 kg mol^{-1}, ΔH (quartz to fused quartz)=0.152 MJ kg^{-1}).

Table S.3. Standard density Kieffer model parameters for stishovite.

Parameter	Value	Source
V_0 [m^3 kg^{-1}]	2.331×10^{-4}	Weidner et al. [1982]
v_1 [m s^{-1}]	5050	Gillet et al. [1990]
v_2 [m s^{-1}]	6190	Gillet et al. [1990]
v_3 [m s^{-1}]	11000	Gillet et al. [1990]
ω_{l} [cm^{-1}]	230	Gillet et al. [1990]
ω_{u} [cm^{-1}]	1020	Gillet et al. [1990]
q_{E}	0	Gillet et al. [1990]
γ_{optic}	0.95	Kieffer [1982]
γ_1	0.59	Kieffer [1982]
γ_2	0.59	Kieffer [1982]
γ_3	2.35	Kieffer [1982]
a_i [K^{-1}]	-3.1(6)$\times 10^{-5}$	this work

Table S.4. Experimental values for Grüneisen parameter in silica fluid.

Source	Volume [10^{-4} m^3 kg^{-1}]	γ
Hicks et al. [2006]	$\leq\sim 1.7$	~ 0.6
Trunin [1994, 1998]	~ 2	0.6 ± 0.1
Lyzenga et al. [1983][a]	2.127	0.75 ± 0.3
McQueen [1992][a]	2.11	1.2
McQueen [1992][b]	1.90	0.4

The sound velocity measurements were reanalyzed using the Hugoniots for (a) fused quartz: Equation 4 in the main text and (b) quartz: Knudson and Desjarlais [2009].

Table S.5. Revised model liquid–vapor curve for silica.

T [K]	P [GPa]	S_{liq} [J kg^{-1} K^{-1}]	S_{vap} [J kg^{-1} K^{-1}]	ρ_{liq} [g cm^{-3}]	ρ_{vap} [g cm^{-3}]
5130	1.32E-01	5149	5149	5.08E-01	5.08E-01
5126	1.31E-01	5074	5224	5.66E-01	4.50E-01
5120	1.29E-01	5030	5269	6.02E-01	4.18E-01
5114	1.27E-01	5002	5301	6.26E-01	3.97E-01
5108	1.25E-01	4979	5327	6.45E-01	3.79E-01
5102	1.23E-01	4956	5350	6.65E-01	3.64E-01
5100	1.23E-01	4949	5355	6.70E-01	3.60E-01
5090	1.20E-01	4919	5388	6.97E-01	3.39E-01
5080	1.17E-01	4892	5416	7.21E-01	3.21E-01
5070	1.14E-01	4870	5443	7.41E-01	3.05E-01
5060	1.11E-01	4846	5467	7.63E-01	2.91E-01
5050	1.08E-01	4827	5489	7.80E-01	2.78E-01
5040	1.05E-01	4806	5509	7.99E-01	2.66E-01
5020	1.00E-01	4771	5550	8.32E-01	2.45E-01
5000	9.49E-02	4740	5586	8.61E-01	2.26E-01
4980	8.99E-02	4711	5621	8.89E-01	2.09E-01
4960	8.52E-02	4682	5652	9.17E-01	1.93E-01
4940	8.07E-02	4657	5683	9.41E-01	1.80E-01
4920	7.64E-02	4621	5700	9.65E-01	1.67E-01
4800	5.42E-02	4495	5858	1.09E+00	1.09E-01
4600	2.94E-02	4337	6084	1.26E+00	5.32E-02
4400	1.52E-02	4199	6272	1.40E+00	2.55E-02
4200	7.60E-03	4077	6440	1.52E+00	1.20E-02
4000	3.64E-03	3966	6597	1.62E+00	5.51E-03
3800	1.66E-03	3861	6749	1.71E+00	2.47E-03
3600	7.10E-04	3759	6901	1.80E+00	1.06E-03
3400	2.80E-04	3659	7061	1.87E+00	4.26E-04
3200	9.97E-05	3559	7233	1.94E+00	1.57E-04
3000	3.12E-05	3457	7425	2.01E+00	5.14E-05
2800	8.29E-06	3354	7645	2.07E+00	1.44E-05
2600	1.79E-06	3248	7904	2.13E+00	3.33E-06
2400	2.98E-07	3135	8211	2.19E+00	5.99E-07
2200	3.51E-08	3018	8590	2.24E+00	7.70E-08
2000	2.68E-09	2946	9247	2.29E+00	6.46E-09

To compare the liquid–vapor curve presented here and that of Melosh [2007], there is a typographical error in Table 3 of Melosh [2007], the parameters for the critical point adjustment are reversed and should read: C53=6×10^{11} dynes cm^{-2} and C54=0.8.